Journal of Fluids and Structures 82 (2018) 492–504

Contents lists available at ScienceDirect

Journal of Fluids and Structures

journal homepage: www.elsevier.com/locate/jfs

On the electrode segmentation for piezoelectric energy harvesting from nonlinear limit cycle oscillations in axial flow

Carlos De Marqui Jr. [a,*], David Tan [b], Alper Erturk [b]

[a] Department of Aeronautical Engineering, Sao Carlos School of Engineering, University of Sao Paulo, Sao Carlos, SP, Brazil
[b] G.W. Woodruff School of Mechanical Engineering, Georgia Institute of Technology, Atlanta, GA 30332, USA

ARTICLE INFO

Article history:
Received 23 January 2018
Received in revised form 23 June 2018
Accepted 31 July 2018

Keywords:
Energy harvesting
Piezoelectricity
Aeroelasticity
Limit cycle oscillations

ABSTRACT

Aeroelastic energy harvesters can be used for low-power electricity generation in various applications ranging from aircraft and rotorcraft to civil structures in high wind areas. Among the various alternative transduction mechanisms for airflow energy harvesting, piezoelectric energy harvesting from limit cycle oscillations of cantilever beams in axial flow has been pointed out as a geometrically scalable and simple option. The dynamic deformed shape of flexible beams during limit cycle oscillations involves more complex motions than simple standing waves and mode shapes. Such deformations yield moving strain nodes (inflection points), where the dynamic bending strain changes sign. As a result, the use of segmented piezoelectric layers to avoid charge cancellation is more involved as compared to modal vibration problems that have fixed strain nodes. To alleviate this issue without implementing complex optimization schemes, this work presents a criterion for segmentation of the piezoelectric layers to enhance the power extraction from aeroelastic limit cycle oscillations of a flexible cantilever in axial flow, based on a cyclic average of the strain node motion. A fluid–structure interaction model that couples the nonlinear governing equations of an electromechanically coupled beam with an unsteady aerodynamic model is implemented, and wind tunnel experiments are performed for validation. Theoretical predictions of the electromechanical response for a piezoelectric bimorph cantilever in axial flow are experimentally validated for both continuous and segmented configurations of the piezoelectric layers. More than 30% enhancement in the electrical power output is observed when piezoelectric layers are segmented based on the criterion given here.

1. Introduction

The literature of energy harvesting exhibits a growing volume of papers toward enabling geometrically scalable and simple flow energy harvesters. The goal is to convert flow energy into usable electrical energy to power small electronic components in applications ranging from health monitoring for aircraft components to wireless sensors located in high wind areas. The conversion of persistent aeroelastic and hydroelastic oscillations of airfoils and hydrofoils (Erturk et al., 2010; Sousa et al., 2011; De Marqui and Erturk, 2013; Dias et al., 2013; Bae and Inman, 2014; Abdelkefi et al., 2012), elastic wings (De Marqui et al., 2010, 2011; Bruni et al., 2017; Xiang et al., 2015) or beams in axial flow (Tang et al., 2009a; Dunnmon et al., 2011; Singh et al., 2012) combined with different transduction mechanisms are among the concepts and configurations investigated in the literature.

* Corresponding author.
E-mail address: demarqui@sc.usp.br (C. De Marqui).

https://doi.org/10.1016/j.jfluidstructs.2018.07.020
0889-9746/

The typical linear flutter behavior is well known from the classical literature of aeroelasticity (Theodorsen, 1935; Bisplinghoff et al., 1996). In that scenario, persistent oscillations occurring at the flutter boundary restrict the operation envelope of a linear flow energy harvester to a single airflow speed. However, real world applications often involve nonlinearities. Nonlinear aeroelastic systems offer persistent oscillations over a range of airflow speeds due to structural nonlinearities (concentrated or distributed) or aerodynamic nonlinearities (Dowell and Tang, 2002). Since the nonlinear aeroelastic behavior is more realistic and also useful for airflow energy harvesting, there has been growing research interest in nonlinear aeroelastic energy harvesters over the past few years (Abdelkefi et al., 2012a; Dunnmon et al., 2011; Sousa et al., 2011; Abdelkefi et al., 2012c; Abdelkefi and Hajj, 2013; Bae and Inman, 2014; Javed et al., 2015; Sousa and De Marqui, 2015).

Early papers discussing the aeroelastic behavior of cantilevers in axial flow assumed linear aeroelastic models and the goal was to investigate the stability of such systems (Kornecki et al., 1976; Shayo, 1980; Huang, 1995; Guo and Paidoussis, 2000). It appears from the literature that Kornecki et al. (1976) presented the first numerical investigation of the axial flutter problem considering a linear beam model combined with Theodorsen's theory for the two-dimensional unsteady aerodynamics. Their work was later extended to a plate formulation combined with Theodorsen's theory to provide a linear aeroelastic model (Shayo, 1980). Huang (1995) presented an experimentally validated linear beam model in axial flow to investigate human snoring that is related to flutter of soft tissue. Guo and Paidoussis (2000) investigated the axial flutter problem considering different structural boundary conditions of a linear beam model and the aerodynamic loads obtained from the direct solution of the potential flow.

Nonlinear aeroelastic behavior of beams in axial flow was first numerically investigated by Tang and Dowell (2002). A nonlinear structural model, which included nonlinearities in stiffness and inertia terms and also the inextensibility condition (Semler et al., 1994), was combined with the three-dimensional unsteady vortex lattice method to provide the nonlinear aeroelastic solution. Tang et al. (2003) presented experimental validations of the nonlinear aeroelastic model of Tang and Dowell (2002). In a series of papers (Tang and Paidoussis, 2007, 2008a, b, 2009; Tang et al., 2009b), the nonlinear aeroelastic behavior of flexible cantilevers in axial flow as well as the effects of different configurations (i.e. external springs, additional concentrated mass, interaction between two cantilevers) are discussed. Tang et al. (2009a) presented a rigorous analysis of the energy transfer from fluid to structure for self-excited vibrations of a cantilever under axial flow when a nonlinear structural model of a cantilever beam was combined with the unsteady lumped vortex method (ULVM). The numerical predictions were experimentally validated via wind tunnel tests of an electromagnetic flow energy harvester (the flutter mill). The authors concluded that arrays of large-scale harvesters could have similar performance of horizontal axis wind turbines. The nonlinear aeroelastic model used in Tang et al. (2009a) for flow energy harvesting purposes was previously presented in Tang and Paidoussis (2007), which was based on the work of Tang and Dowell (2002), showing that similar modeling assumptions have been employed by different authors.

Piezoelectric energy harvesting from nonlinear limit cycle oscillations (LCO) of a cantilever beam in axial flow was first discussed in Dunnmon et al. (2011). The equations of motion from Tang and Dowell (2002) were combined with linear piezoelectricity (Erturk and Inman, 2008), resulting in an electromechanically coupled nonlinear structural model (Dunnmon et al., 2011). The unsteady aerodynamic loads were obtained from the unsteady vortex lattice method. Experimental validations and also efficiency measures were reported in order to characterize the flow energy harvesting system. Pineirua et al. (2015) presented the optimization problem of electrodes configuration (position and dimensions along the length) of a nonlinear beam in axial flow for piezoelectric energy harvesting. Considering numerical results from a weakly nonlinear model and experimental data, they (Pineirua et al., 2015) discussed the numerical optimization of the energy flow among the fluid, structure, and electrical domains of the problem in three different configurations. For each case, the optimum electrode configuration was determined from the analysis of numerical results considering the effects of different parameters on the electroaeroelastic behavior the system. In a recent paper, Tang and Dowell (2018) presented a new inextensible nonlinear plate structural model that was combined with an electromechanical model and a rotated unsteady vortex lattice method to investigate the behavior of a piezoelectric laminated plate as the yaw angle between the clamped end and airflow direction changed.

In the current work, we present an experimentally validated simple criterion for electrode segmentation in order to reduce cancelation of electrical output from LCOs of flexible beams in axial flow. First, nonlinear aeroelastic model predictions for a plain flexible steel beam in axial flow are validated against wind tunnel results. The analysis of the aeroelastic response, particularly the dynamic strain distribution during LCOs within a cycle at different post-critical airflow speeds (i.e. at speeds above the critical speed), yields a criterion for segmentation of the electrodes (or of the piezoelectric material). Theoretical predictions of the electrical power output of a piezoelectric bimorph cantilever (PVDF - polyvinylidene fluoride- bimorph with steel substrate) in axial flow are experimentally validated for both continuous and segmented configurations of the piezoelectric layers, and performance enhancement via electrode segmentation is quantified.

2. Nonlinear aeroelastic model with piezoelectric coupling

From the aeroelastic side, the modeling approach employed in this work is similar to the ones presented by Tang and Dowell (2002), Tang and Paidoussis (2007), Tang et al. (2009a), and Dunnmon et al. (2011). As reviewed in the previous section, similar modeling assumptions have been employed in investigating the aeroelastic behavior of nonlinear flexible cantilevers in axial flow. Fig. 1(a) displays a cantilevered flexible piezoelectric beam of length L and width b in uniform

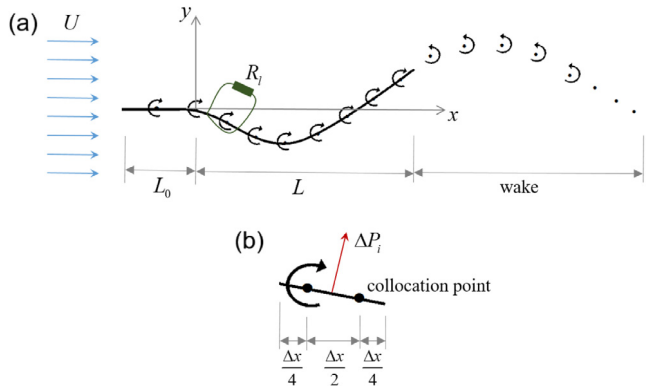

Fig. 1. **(a)** Flexible cantilever (energy harvester with piezoelectric layers) under axial flow and **(b)** a representative aerodynamic panel.

axial flow. The cantilever is a symmetric bimorph (Erturk and Inman, 2011) (a metallic substructure sandwiched by two PVDF layers) connected in series to a load resistance. The piezoelectric layers (which are poled oppositely in the thickness direction) completely cover the substructure. The mass density of the substructure is ρ_s and its thickness is h_s. The mass density of the piezoelectric material is ρ_p and the thickness of each piezoelectric layer is h_p. The undisturbed airflow speed is U and the segment L_o at the upstream end of the beam takes into account the clamping device that is also exposed to the airstream. The mass density of the fluid is ρ_F.

For the structural modeling of an electromechanically coupled cantilever in axial flow, Hamilton's principle is employed:

$$\int_{t_1}^{t_2} [\delta(T - V + W_e) + \delta W]dt = 0 \tag{1}$$

where T is the kinetic energy, V is the potential energy, W_e is the electrical energy, and δW is the virtual work related to the aerodynamic loads (to be described later in this section) and the electrically extracted work due to the load resistance.

Axial inextensibility is assumed for the planar motion of the beam such that:

$$\left(1 + \frac{\partial u}{\partial x}\right)^2 + \left(\frac{\partial w}{\partial x}\right)^2 = 1 \tag{2}$$

where u is the longitudinal displacement and w is the transverse displacement of the beam at position x and time t.

The kinetic energy of the beam is then

$$T = \frac{1}{2} m \int_0^L \left(\dot{u}^2 + \dot{w}^2\right) dx \tag{3}$$

where $m = \rho_s h_s + 2\rho_p h_p$. The potential energy of the beam is

$$V = \frac{1}{2} \int_0^L D\Psi''^2 dx + \frac{1}{2} \int_{V_p} T_1 S_1 dV_p \tag{4}$$

where D is the bending stiffness of the overall composite beam. The axial stress and strain along the length of the beam are T_1 and S_1, respectively, and V_p is the volume of the piezoelectric layers. Linear-electroelastic behavior is assumed for the piezoelectric material. Therefore, $T_1 = \overline{c}_{11}^E S_1 - \overline{e}_{31} E_3$ where $\overline{c}_{11}^E$ is the reduced elastic stiffness of the piezoelectric material measured at constant electric field, $\overline{e}_{31}$ is the reduced piezoelectric stress constant (both are defined for the thin structure), and E_3 is the non-zero electric field component (in transverse direction since the piezoelectric layers are assumed poled in the thickness direction) (Erturk and Inman, 2011). The nonlinear curvature in Eq. (4) is (Semler et al., 1994)

$$\Psi''^2 \approx \left(\frac{\partial^2 w}{\partial x^2}\right)^2 \left[1 + \left(\frac{\partial w}{\partial x}\right)^2\right] \tag{5}$$

for $(\partial w/\partial x)^2 \ll 1$.

The internal electrical energy is

$$W_e = \frac{1}{2} \int_{V_p} D_3 E_3 dV_p \tag{6}$$

where D_3 is the electric displacement (in the thickness of the piezoelectric layers). Since linear piezoelectricity is considered in this work, $D_3 = \overline{e}_{31} S_1 + \overline{\varepsilon}_{33}^S E_3$ where $\overline{\varepsilon}_{33}^S$ is the reduced permittivity of the piezoelectric material evaluated at constant strain (Erturk and Inman, 2011) for a thin structure.

For a set of applied aerodynamic loads Δp, and for a set of discrete electric charge outputs q_e, the first variation of mechanical work and electrically extracted work is

$$\delta W = \sum_{i=1}^{nf} \delta w(x_i, t)\Delta p(x_i, t) + \sum_{j=1}^{nq} \delta\varphi(x_j, t)q_e(x_j, t) \tag{7}$$

where nf is the number of applied mechanical forces, nq is the number of discrete electrodes pairs, and φ is the respective electric potentials.

Performing the variational operations on Hamilton's principle (Tang and Dowell, 2002), taking into account the inextensibility condition (Eq. (2)), and assuming a Kelvin–Voigt damping model (for the structure), one can obtain the electromechanically coupled equations of the system as

$$m\ddot{w} + D\left(1 + a\frac{\partial}{\partial t}\right)\left[\frac{\partial^4 w}{\partial x^4}\left(1 + \left(\frac{\partial w}{\partial x}\right)^2\right) + 4\frac{\partial w}{\partial x}\frac{\partial^2 w}{\partial x^2}\frac{\partial^3 w}{\partial x^3} + \left(\frac{\partial^2 w}{\partial x^2}\right)\right]$$
$$- \frac{\partial^2 w}{\partial x^2}\int_s^L\int_0^x m\left(\left(\frac{\partial \dot{w}}{\partial x}\right)^2 + \frac{\partial w}{\partial x}\frac{\partial \ddot{w}}{\partial x}\right)dxdx + \frac{\partial w}{\partial x}\int_0^x m\left(\left(\frac{\partial \dot{w}}{\partial x}\right)^2 + \frac{\partial w}{\partial x}\frac{\partial \ddot{w}}{\partial x}\right)dx - \theta v_p\left(\frac{d\delta(x)}{dx} - \frac{d\delta(x-L)}{dx}\right) = F \tag{8}$$

$$C_p\dot{v}_p + \frac{v_p}{R_l} + \theta\int_0^L \frac{\partial^2 \dot{w}}{\partial x^2}dx = 0 \tag{9}$$

where a is the damping coefficient, θ is the electromechanical coupling, C_p is the equivalent capacitance, v_p is the voltage across the electrodes, R_l is the resistive load, $\delta(x)$ is the Dirac delta function, an over-dot represents differentiation with respect to time, and F is defined as

$$F = F_L - \frac{\partial w}{\partial x}F_D + \frac{\partial^2 w}{\partial x^2}\int_x^L F_D dx \tag{10}$$

where F_L is the transverse fluid load acting on the body and F_D is the longitudinal fluid load acting on the body.

The aerodynamic loads in Eqs. (8)–(10) are obtained using the ULVM (Tang and Dowell, 2002; Katz and Plotkin, 2001). The flexible beam and the wake are divided into panels (Fig. 1(a)) with a lumped vortex element placed at the quarter chord point of each panel and the collocation point placed at the three quarter chord of each panel as depicted in Fig. 1(b). After shedding from the body, the vortices move via the convection effect as a result of the velocity induced by other vortices. The boundary conditions (zero normal flow) are verified at the three quarter chord position of each panel (Fig. 1(b)). At each time step, the strength of each vortex placed on the panels along the body length is obtained. The transverse and longitudinal forces at each panel are

$$F_{L_i} = \Delta P_i \cos\alpha_i \tag{11}$$
$$F_{D_i} = \Delta P_i \sin\alpha_i \tag{12}$$

where ΔP_i is the pressure difference across the ith panel and α_i is the angle of incidence of the ith panel (Fig. 1(b)). A detailed description of the ULVM applied to the axial flow problem can be found in Tang and Dowell (2002).

The transverse displacement w is expanded as,

$$w(x, t) = \sum_{m=1}^{N} q_m(t)\phi_m(x) \tag{13}$$

where $\phi_m(x)$ is obtained from the linearized solution as the eigenfunctions (i.e. mode shapes). Note that the linear mode shapes properly describe the actual nonlinear mode shapes of a beam up to quite large amplitudes (Shang-Rou et al., 1994). Substituting Eq. (13) into Eqs. (8) and (9), multiplying by $\phi_i(x)$ and integrating over the length results in the equations

$$M_{ii}\ddot{q}_i + \omega_i^2 M_{ii}q_i + a\omega_i^2 M_{ii}\dot{q}_i + B_{inrs}q_n q_r q_s + aB_{inrs}\left(\dot{q}_n q_r q_s + q_n\dot{q}_r q_s + q_n q_r\dot{q}_s\right)$$
$$+ C_{inrs}q_n\left(\dot{q}_r\dot{q}_s + q_r\ddot{q}_s\right) - \Theta_i v_p = f_i \tag{14}$$

$$C_p\dot{v}_p + \frac{v_p}{R_l} + \Theta_i\dot{q}_i = 0 \tag{15}$$

here, q_i is the generalized displacement of the ith structural mode normalized by L (overhang length of the beam), M_{ii} is an element of the mass matrix, Θ_i is an element of the generalized electromechanical coupling vector, and $f_i = \int_0^1 \phi_i(x)Fdx$. The constant coefficients in Eqs. (14) and (15) are

$$B_{inrs} = \int_0^1 D\phi_i\left(\phi_n''''\phi_r'\phi_s' + 4\phi_n'\phi_r''\phi_s''' + \phi_n''\phi_r''\phi_s''\right)dx \tag{16}$$

$$C_{inrs} = \int_0^1 m_p\phi_i\phi_n'\left(\int_0^x \phi_r'\phi_s' dx\right)dx - \int_0^1 m_p\phi_i\phi_n''\left(\int_x^1\int_0^x \phi_r'\phi_s' dxdx\right)dx \tag{17}$$

where the prime represents differentiation with respect to length of the body. The expressions for the equivalent capacitance and modal electromechanical coupling of the piezoelectric bimorph (series connection) are

$$C_p = \frac{\varepsilon_{33}^s bL}{2h_p} \tag{18}$$

$$\Theta_i = \frac{\bar{e}_{31} b}{2h_p}(h_d^2 - h_e^2)\int_0^1 \frac{d^2\phi_i(x)}{dx^2}dx \tag{19}$$

where h_d and h_e are the distances from the neutral axis of the composite cross-section to the outer and inner electrodes of the piezoelectric layers, respectively. In the case of the bimorph in this work, in addition to the effects of the piezoelectric layers, the thickness of each epoxy layer (used in bonding) is considered in the calculation of the electromechanical coupling, mass, and bending stiffness of the composite section.

In the case of a passive beam (first case study in the following), only the electrically uncoupled version of Eq. (14) is taken into consideration. In the presence of piezoelectric coupling (second case study), a bimorph in series cantilever (a plain steel beam sandwiched by two layer of PVDF) is investigated for energy harvesting. Note that the nonlinear aeroelastic phenomenon is not significantly affected by the resistive shunt damping effect of piezoelectric power generation since piezoelectric coupling is relatively weak in flexible structures, such as the PVDF-based flexible cantilever considered in this work. Therefore, one-way coupling can be assumed in Eqs. (14) and (15) for the simulation of the piezoaeroelastic behavior of the cantilever bimorph in axial flow by neglecting the voltage term in the mechanical equation. Moreover, the dimensionless and electromechanically uncoupled version of Eq. (14) is

$$\ddot{q}_i + A_i q_i + \alpha A_i \dot{q} + B_{imnl} q_m q_n q_l + \alpha B_{imnl}\left(\dot{q}_m q_n q_l + q_m \dot{q}_n q_l + q_m q_n \dot{q}_l\right) + C_{imnl} q_m\left(\dot{q}_n \dot{q}_l + q_n \ddot{q}_l\right) = f_i \tag{20}$$

where the dimensionless damping coefficient is

$$\alpha = \frac{a}{\sqrt{\frac{mL^4}{D}}} \tag{21}$$

and

$$A_i = \lambda_i^4 \tag{22}$$

$$B_{inrs} = \int_0^1 \phi_i\left(\phi_n'''' \phi_r' \phi_s' + 4\phi_n' \phi_r'' \phi_s''' + \phi_n'' \phi_r'' \phi_s''\right) dx \tag{23}$$

$$C_{inrs} = \int_0^1 \phi_i \phi_n' \left(\int_0^x \phi_r' \phi_s' dx\right) dx - \int_0^1 \phi_i \phi_n'' \left(\int_x^1 \int_0^x \phi_r' \phi_s' dx dx\right) dx. \tag{24}$$

Here, λ_i is the dimensionless eigenvalue of the i^{th} mode of the structure. Moreover, the generalized dimensionless aerodynamic load is modified as,

$$f_i = \mu U_R^2 \int_0^1 \left\{f_L - w' f_D + w'' \int_s^1 f_D ds\right\} \phi_i ds \tag{25}$$

where $f_L = F_L/\rho_F U^2$ and $f_D = F_D/\rho_F U^2$. The mass ratio is defined as $\mu = \rho_F L/m$ and the dimensionless airflow speed is $U_R = UL\sqrt{m/D}$. The response of the bimorph cantilever in axial flow is predicted by solving Eq. (14) (for weak electromechanical coupling) or its dimensionless version (Eq. (20)), in order to obtain the generalized displacements at a certain airflow speed, and then the electrical output is directly solved using Eq. (15). The numerical solution of the governing equations follows the procedure adopted in Tang and Paidoussis (2007). In this approach, the Houbolt method (Houbolt, 1950) (based on a two multistep backward finite-difference approximation) is employed to solve the governing nonlinear equations.

3. Theoretical and experimental results

This section presents the theoretical and experimental investigations of a cantilever in axial airflow excitation. First, the numerical simulations for nonlinear aeroelastic behavior of a plain steel beam (cut-in speed of LCO and resulting deformation shape) are validated against wind tunnel experiments for various airflow speeds. The analysis of the dynamic strain distribution during LCOs at different post-critical airflow speeds results in a criterion for the segmentation of electrodes (or piezoelectric materials) to minimize charge cancellation. Finally, numerical predictions of the voltage output and power output of a piezoelectric bimorph cantilever (PVDF bimorph with steel substrate) in axial flow are experimentally validated for continuous and segmented piezoelectric cases, and performance enhancement is validated.

3.1. Experimental setup and model validation

Fig. 2(a) shows the physical setup for the plain steel beam in axial flow. The beam is made from tempered stainless steel with mass density of 7880 kg/m^3 and Young's modulus 210 GPa. The overhang length of the beam for the experimental model

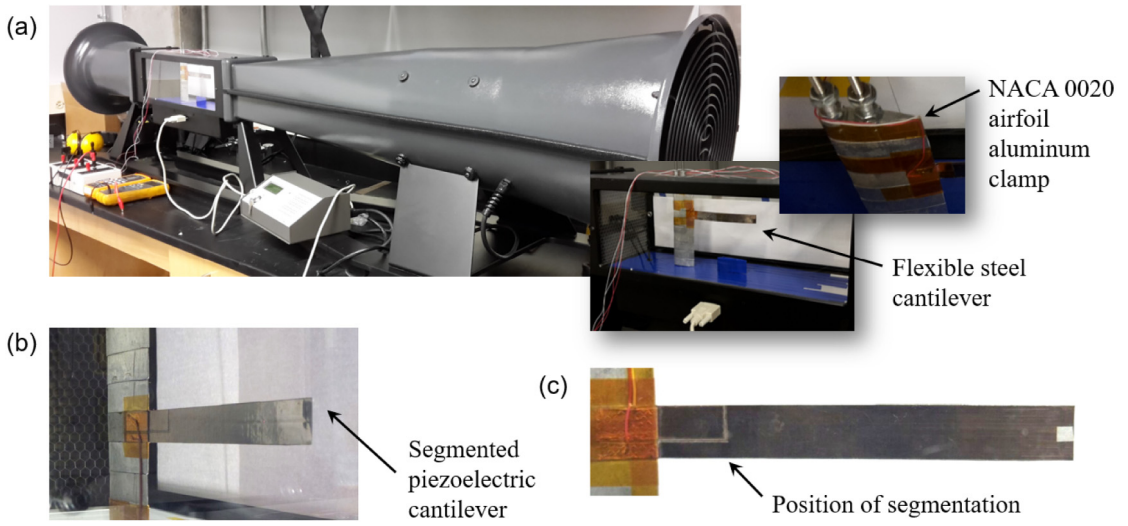

Fig. 2. **(a)** Experimental setup showing the details of the test section and the airfoil clamp; **(b)** PVDF bimorph energy harvester in the test section and **(c)** a close-up showing the position of segmentation.

and numerical simulations is 66.5 mm, its width is 12.7 mm and thickness is 76.2 μm. The mass ratio (defined previously) is 0.14 for the air density of 1.225 kg/m^3. Structural damping ratios (for low amplitudes) were obtained using a vacuum setup where the tip velocity frequency response function (beam tip velocity per base acceleration) is measured (Fig. 3 — note from the figure that, even in the absence of airflow, structural damping identification of a flexible cantilever in air would be very inaccurate; therefore, in vacuo testing is necessary, which is often overlooked). The damping ratios were identified as 0.0017 and 0.0004 for modes 1 and 2, respectively, using the half-power method. The flexible beam is clamped into a rigid airfoil support made of solid aluminum with a NACA 0020 section. The chord length of the airfoil section (clamp) is 38.1 mm and the span is the total height of the wind tunnel test section.

The wind tunnel is a Jet Stream 500 model with a 450 mm long test section that has a cross section of 130 mm x 130 mm. The average wind tunnel flow velocity was measured by using a conventional Pitot tube. In the simulations, the overhang length of the cantilever was divided into 200 aerodynamic segments while the length of the wake is assumed as 50 body lengths, and eight structural modes were considered. Since the damping ratios and resonance frequencies were experimentally identified for modes 1 and 2 (Fig. 3), the proportionality constants and, therefore, damping ratios for higher modes can be determined (Erturk and Inman, 2008), or alternatively these modal damping ratios can also be experimentally identified. In the experiments, a high-speed camera system (Phantom v7.3 Vision Research) was used to extract the vibration response of the entire cantilever during the LCOs in the post-critical condition. Analysis of each recorded video (at each airflow speed) resulted in sufficient number of data points extracted from the deformation shape of the beam. The measured deformation shape is used to validate model predictions.

Fig. 4 shows the theoretically predicted and experimentally measured displacement amplitude at the free end of the beam over a range of airflow speeds. The nonlinear aeroelastic model predicts that the critical airflow speed for the onset of LCO is slightly above 24.0 m/s, while the experimental critical speed is 25.9 m/s and is rather abrupt (which agrees with results in Dunnmon et al., 2011). For airflow speeds smaller than the critical one, the system is stable and any small disturbance is attenuated. For airflow speeds above the critical speed, large amplitude LCOs are observed. The model predictions are in good agreement with the experimentally obtained amplitudes for airflow speeds slightly larger than the critical one (where the theoretical and experimental tip displacement increase with similar slopes). However, the experimentally measured tip displacement becomes less sensitive to the variation of airflow speed for larger airflow speeds while theoretical tip displacement increases with increasing airflow speed. Although the model considers nonlinear structural terms (and the slope of tip displacement with increasing airflow speed is not constant for the considered range of airflow speeds), the aerodynamic model assumes two-dimensional theory based on potential flow and small disturbance motion. On the other hand, the experimental setup presents significant three-dimensional effects (e.g. vortex shedding from the sides of the beam) and, eventually, flow separation after certain amplitude of motion. Even in the absence of flow separation, boundary layer effects with increasing airflow speed (thicker layer and adverse velocity gradient observed before the occurrence of flow separation) can lead to smaller aerodynamic loads (as would be observed for smaller structural displacements), which is not included in the assumed aerodynamic model. Therefore, after a certain airflow speed, the theoretical aerodynamic loads can be larger than the experimental ones, overestimating experimental tip displacement. Another source of mismatch between the theoretical model and the experimental setup is the finite dimensions of the test section of the small wind tunnel and potential aerodynamic interactions between the cantilever and test section walls.

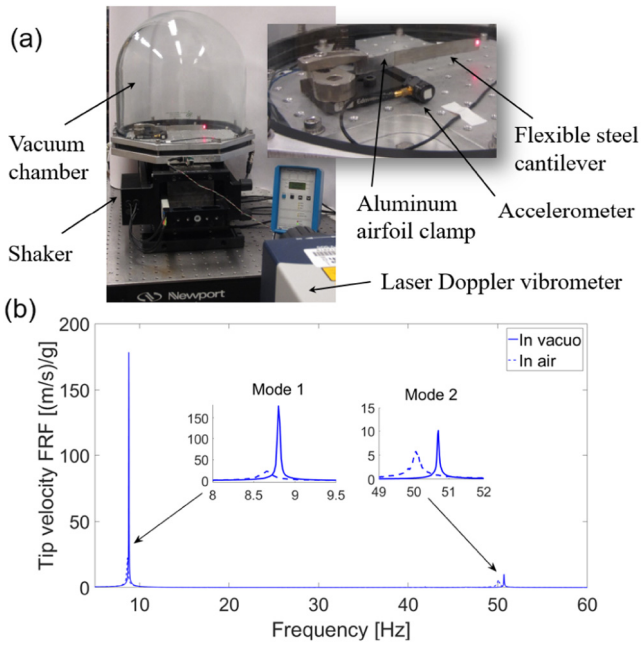

Fig. 3. **(a)** In vacuo base excitation setup and **(b)** linear frequency response functions (for the steel cantilever) based on zero airflow speed base excitation experiments for in air and in vacuo conditions (in vacuo data is employed for modal damping identification).

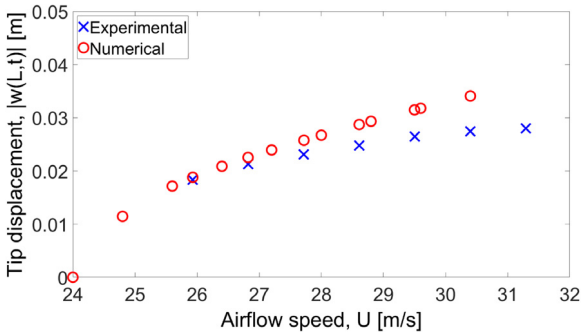

Fig. 4. Theoretical and experimental transverse tip displacement amplitudes of the flexible steel cantilever for various airflow speeds in the post-critical range.

Fig. 5(a) to (c) display the deformation shapes along one cycle of oscillation of LCO for the airflow speeds of 25.9 m/s, 28.6 m/s and 30.4 m/s, respectively. Fig. 5(a) shows good agreement between theoretical prediction (continuous lines) and experimentally measured (markers) beam deflection shape for the airflow speed of 25.9 m/s (experimental onset of LCOs). For the airflow speeds of 28.6 m/s and 30.4 m/s shown in Fig. 5(b) and (c), the model overestimates the maximum tip displacement (in agreement with the discussion presented for Fig. 4). Overall, the predicted deformation shapes are very similar to the experimental ones for all LCO speeds considered in this work, which serves as a validation of the aeroelastic model and numerical solution for a passive structure.

3.2. Strain node motion and electrode segmentation

Linear vibration modes (other than the fundamental mode) of a cantilevered beam have certain strain nodes where the dynamic bending strain distribution changes sign along the length of the beam (Erturk et al., 2009). In standing wave problems of modal vibrations and persistent harmonic excitation, the positions of the strain nodes for each mode are stationary. Since the integrand of Eq. (19) is the curvature eigenfunction (that is related to the dynamic bending strain), covering the inflection points of an electromechanically coupled beam with continuous electrodes results in reduced electromechanical coupling and consequently reduced electrical output in energy harvesting (Erturk et al., 2009). Electrode

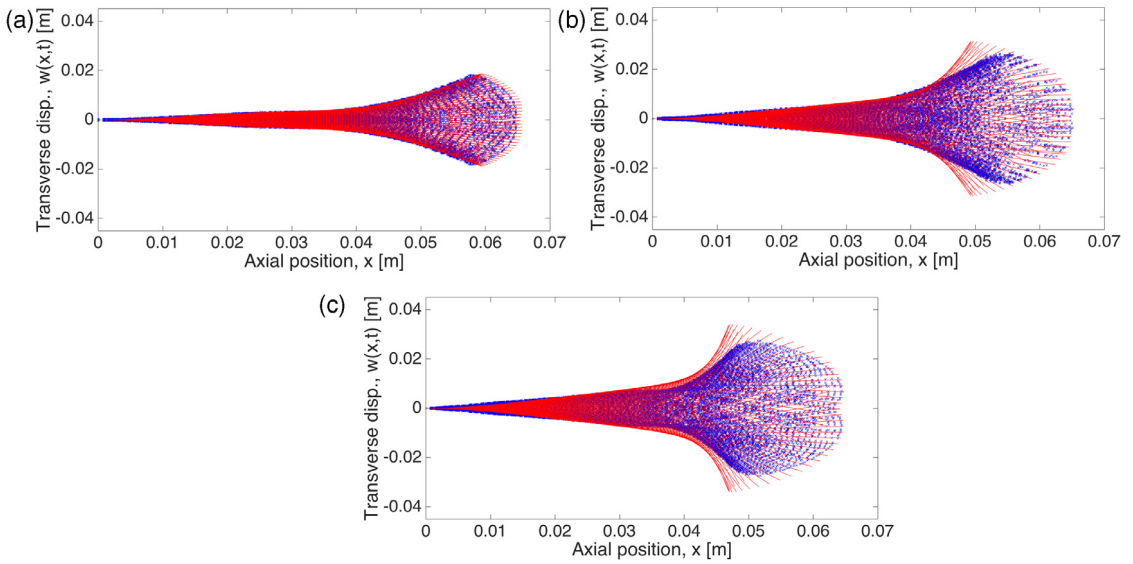

Fig. 5. Theoretical (continuous lines) and experimental (markers) beam deformation shapes in one cycle of oscillation for the airflow speeds of **(a)** 25.9 m/s, **(b)** 28.6 m/s, and **(c)** 30.4 m/s.

and/or piezoelectric layer segmentation at the strain node(s) of a target mode for collecting the electric charge separately and then properly combining eliminates the cancellation problem in simple vibration problems.

Unlike direct harmonic excitation and standing wave problems of beams, strain nodes of aeroelastic deformations are not fixed, i.e. they move along the structure within a cycle of oscillation. Therefore, piezoelectric (or electrode) layer segmentation to avoid cancelations problems is more involved. In Fig. 5 (as well as for the entire range of post-critical airflow speeds of Fig. 4) the modal content of the LCO does not contain only a single mode, but time-varying combinations of modes that are predominantly comprised of the first and the second vibration modes as compared to higher modes.

Fig. 6(a)–(c) displays the numerically calculated curvature distribution in one cycle of oscillation of the nonlinear beam in axial flow for the airflow speeds of 25.9 m/s, 28.6 m/s, and 30.1 m/s. The round markers show the extreme positions of the strain nodes during one cycle of persistent oscillations at each airflow speed (excluding relatively flat deformations that lead to small contribution to the electrical output during one cycle of oscillation). Fig. 6(d)–(f) shows the spatial location of the strain node along the beam length for a half cycle, revealing that it is not in a fixed location relative to the length of the beam during each cycle of persistent oscillation at each airflow speed. One should note, however, that the strain node is mostly placed in a specific region during one cycle of oscillation (where the slope is relatively low in Fig. 6(d)–(f)) at each specific airflow speed. In this work, the dominant position of the strain node during one cycle of oscillation of each airflow speed (which is numerically verified since the strain node position is known at each time step) is averaged over a range of airflow speeds to obtain the position for electrode/piezoelectric segmentation (reducing the charge cancelation due to Eq. (19) in each cycle of oscillations). Based on this approach, according to Fig. 6, the averaged position for segmentation is 17% of the beam length (from the clamped end). Energy harvesting results for this criterion are shown next for continuous and segmented piezoelectric beams under axial flow.

3.3. *Energy harvesting results*

This section provides the numerical demonstration and experimental validation of the segmentation criterion discussed in the previous section. A bimorph in series configuration (two PVDF layers sandwiching a steel substrate) is considered in the numerical simulations and wind tunnel tests both in continuous and in segmented piezoelectric configurations (Fig. 2(b)). The continuous PVDF is obtained by electrically combining both the short and long segments of the segmented PVDF beam displayed in Fig. 2(c) in parallel without reversing the wires. The same wind tunnel setup described in Fig. 2(a) was employed to test the composite piezoelectric beam. The overhang length of the electromechanically coupled beam is 0.1 m and the width is 12.7 mm. The thickness of the steel substrate is the same as the previous section (76.2 μm). The PVDF layers completely cover the overhang area of the beam and the thickness of each PVDF layer is 52 μm. The mass density of PVDF is 1780 kg/m^3 and the elastic modulus is 4 GPa. The thickness of each epoxy layer (in between the substrate and each PVDF layer) is around 12 μm (estimated since the thickness of the bimorph – measured with a micrometer – and the thicknesses of the substructure and PVDF were known). The mass density and elastic modulus of epoxy are 1000 kg/m^3 and 2 GPa, respectively. Structural damping ratios (for low amplitudes) were obtained using a vacuum experimental setup (as in Fig. 3) and identified as 0.0028 and 0.0021 for the first and the second bending modes, respectively. The permittivity of the PVDF

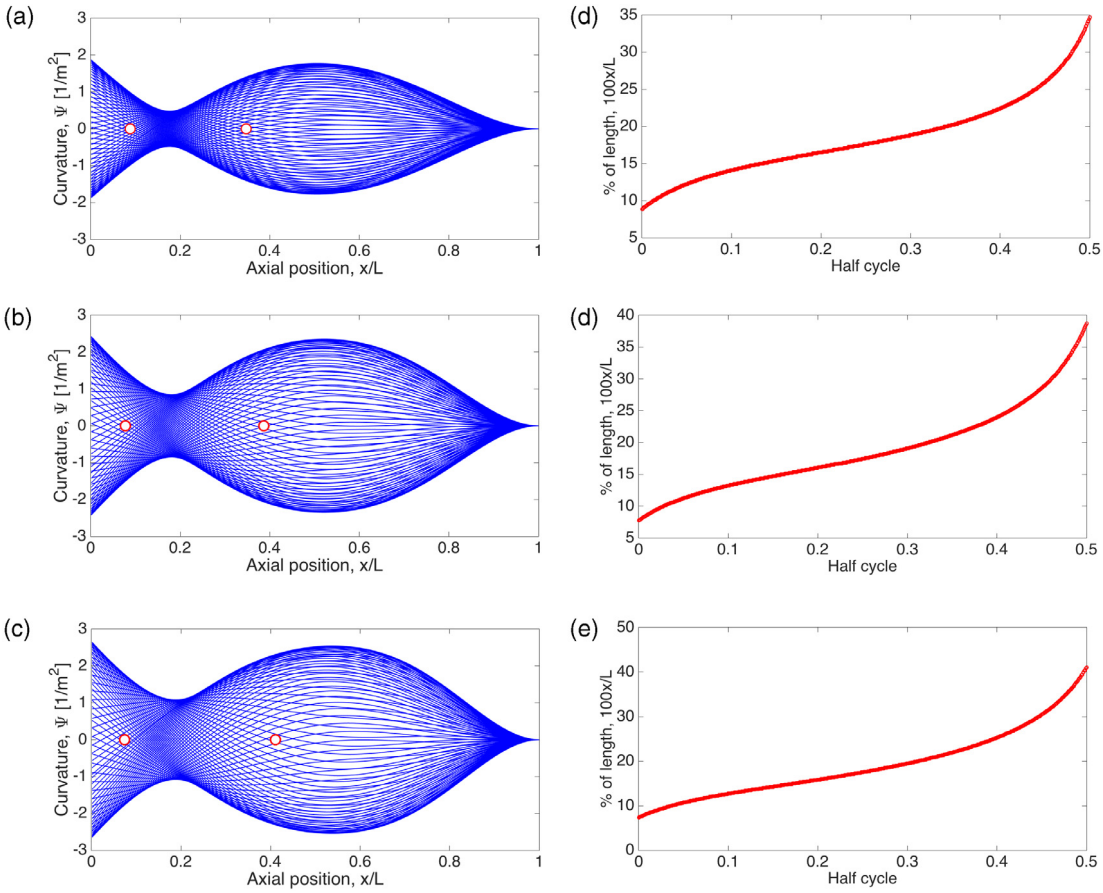

Fig. 6. Curvature of the beam (normalized by length) and spatial position of the strain node during a half cycle of oscillation for the airflow speeds of **(a)** 25.9 m/s, **(b)** 28.6 m/s, and **(c)** 30.4 m/s.

at constant stress is $\varepsilon_{33}^{T} = 110$ pF/m and the piezoelectric strain constant is $d_{31} = 28$ pC/N. Overall, this composite beam is longer but also thicker than the previous plain steel beam case analyzed previously.

Although the composite piezoelectric cantilever has different dimensions (thickness and length) and properties (structural mass and bending stiffness) as compared to the plain steel beam of the previous section, one should note that the mass ratio ($\mu = \rho_F L/m$) is similar in both cases (0.14 and 0.15 for the plain steel beam and composite PVDF beam, respectively). Tang and Paidoussis (2007) discuss the effects of dimensionless parameters on the nonlinear aeroelastic behavior of cantilevers in axial flow. The dimensionless damping coefficient and dimensionless length of the clamped section slightly modify the critical airflow speed and the amplitude of LCO. However, the aeroelastic behavior is strongly modified by the mass ratio of the system. They (Tang and Paidoussis, 2007) report that, with increased mass ratio higher modes are also included in the deformation shape of LCOs. On the other hand, systems with similar mass ratios have similar dimensionless critical speed as well as similar deformation shapes during LCOs. Therefore, the segmentation position defined in the previous section (17% of the length from the clamped end) is employed in the present case (which would apply to other configurations with similar mass ratios). For a system with a significantly different mass ratio, the analysis given in the previous section should be performed and one might have more than one segmentation points depending on the deformation shape.

Fig. 7 shows the theoretically predicted and experimentally measured voltage outputs of the bimorph in series beam considering the segmented piezoelectric layers. The segmentation performed at 17% of the length results in a short segment (from the clamped end to 17% of the length) and a long segment (from 17% of the length to the free end of the beam) as shown in Fig. 2(c). To explore the behavior in open-circuit condition, each segment was connected to a load resistance of 210 MΩ. In the segmented configuration, the electromechanical coupling of each segment and for each mode considered in the simulations is also calculated using Eq. (19). However, the integration limits range from the clamped end to $0.17L$ for the short segment and from $0.17L$ to L for the long segment. Moreover, the length of the short segment has to replace L in Eq. (18) to calculate the capacitance of the short segment while L has to be replaced by $0.83L$ (which is modified in the experiments due to the extension toward the clamp) to obtain the capacitance of the long segment (yielding two circuit equations). The critical airflow speed for the onset of LCO is predicted as 30.5 m/s and the experimental critical speed is

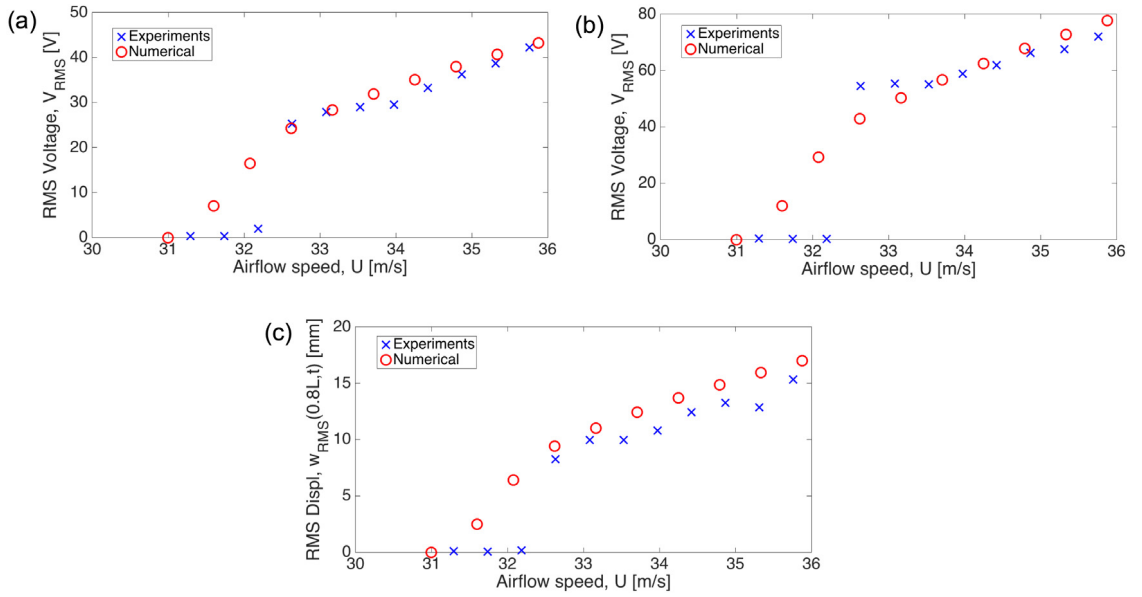

Fig. 7. Theoretical and experimental results of the segmented PVDF bimorph in the post-critical regime and open circuit condition for **(a)** voltage output of the short segment, **(b)** voltage output of the long segment, and **(c)** transverse displacement at 80% of the length from the clamped end.

32.5 m/s (large amplitude LCO). As shown in Fig. 7(a), the theoretically predicted open-circuit voltage output from the short segment is in good agreement with the experimental data. As demonstrated in Fig. 5, the model successfully predicts the displacement amplitudes around the clamped end of the cantilever and, therefore, a good agreement of voltage outputs is no surprise. Fig. 7(b) shows that the model overestimates the voltage output from the long segment, analogous to the results and discussion of Fig. 5. Fig. 7(c) shows the predicted and experimentally measured displacement amplitude at 80% of the overhang length (from the clamped end) of the composite beam. A good agreement between the theoretical and experimental displacements is observed, in agreement with the analysis presented in Fig. 5 for the plain cantilever.

Fig. 8 displays the theoretical and experimental voltage output results for the segmented PVDF case (short segment and long segment in Fig. 8(a) and (b), respectively) and for the continuous PVDF case (Fig. 8(c)) at an airflow speed of 34 m/s for a set of load resistances. The voltage output increases with increasing load resistance from short-circuit to open-circuit condition. Fig. 8(a) shows a good agreement between model predictions and experimental data for the short segment, while Fig. 8(b) shows that the model overestimates the experimental voltage output from the long segment, in agreement with the previous discussions with Fig. 5. The theoretical model slightly overestimates the experimental results of the continuous PVDF case (Fig. 8(c)).

Figs. 7 and 8 show a good agreement between the model predictions and experimental results for changing airflow speed in open-circuit condition and also for a specific airflow speed with changing load resistance, respectively. Although Fig. 8 shows that voltage output from the long segment is always larger than the voltage output from the continuous PVDF case, the benefits of the segmentation criterion given in this work can only be addressed through electrical power output analysis. Fig. 9(a) and (b) show the theoretical and experimental electrical power output for the short and long segments of the PVDF beam, respectively, while Fig. 9(c) shows the power output for the continuous PVDF case at the same airflow speed and for the same set of load resistance values considered in Fig. 9. One should note that piezoelectric coupling is indeed weak in this axial flutter problem for a PVDF cantilever; as a result, the optimum load resistance for each case is around $1/\omega C_p$ (where each segment, as well as the continuous case, has its own capacitance). This observation confirms that the one-way electromechanical coupling assumption is valid. Moreover, for the airflow speed considered in Figs. 8 and 9, the simple segmentation criterion given in this work yields an average power output (by adding the maximum power output of each segment in Fig. 9(a) and (b)) that is more than 30% the average power output of the continuous PVDF case.

4. Conclusions

Segmentation of electrodes and/or piezoelectric layers for enhanced energy harvesting from axial flow is explored in this paper. An aeroelastic model is implemented by combining a nonlinear beam model, which takes into account nonlinear inertia and nonlinear curvature terms, an unsteady aerodynamic model, and linear piezoelectric coupling with a load resistance. The nonlinear model predictions for a flexible plain steel beam, which include the cut-in speed of LCOs and the deformation shape of the beam during LCOs, are successfully validated against experimental wind tunnel data. Although the predicted deformations during LCOs are in good agreement with the experimental ones for airflow speeds slightly larger

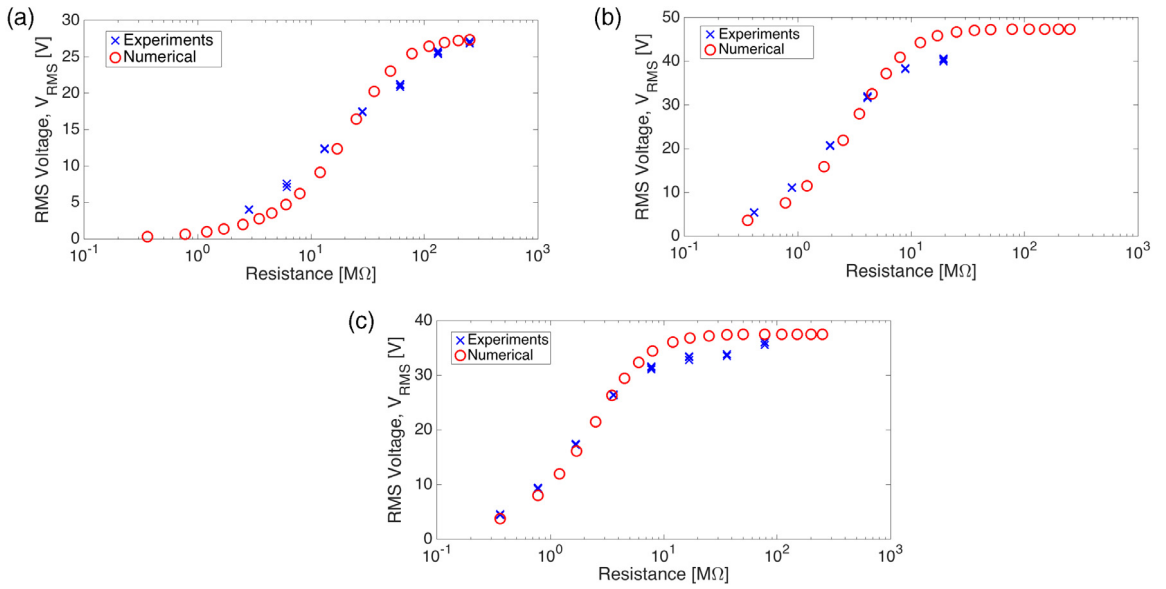

Fig. 8. Theoretical and experimental voltage output of the PVDF bimorph for a set of load resistances at the airflow speed of 34 m/s for **(a)** short segment, **(b)** long segment, and **(c)** continuous piezoelectric layers.

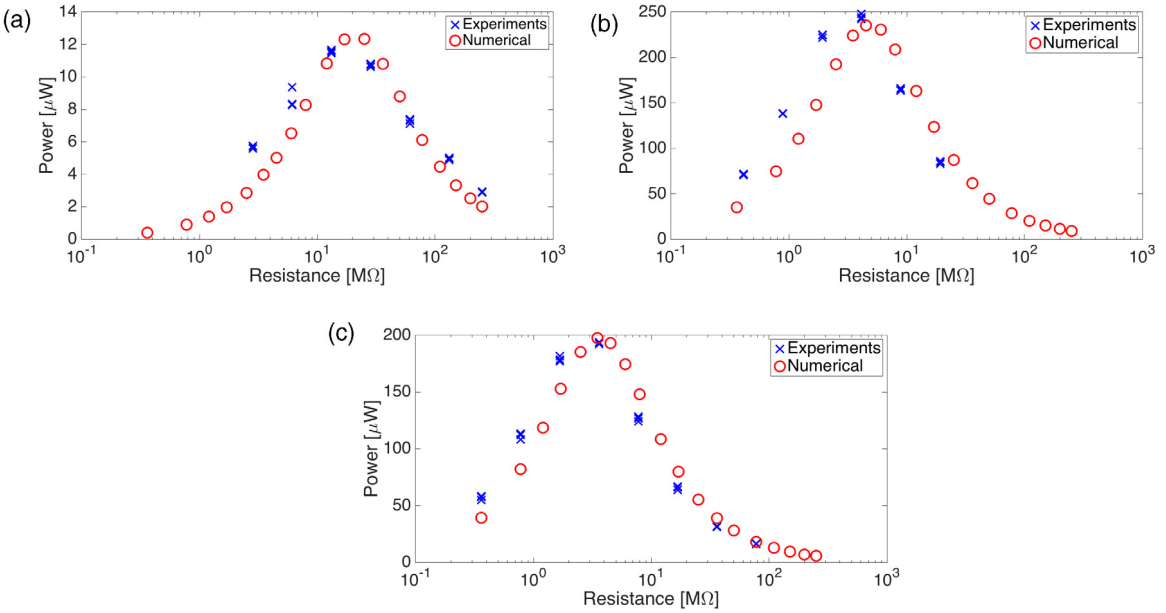

Fig. 9. Theoretical and experimental average power output of the PVDF bimorph for a set of load resistances at the airflow speed of 34 m/s for **(a)** short segment, **(b)** long segment, and **(c)** continuous piezoelectric layers.

than the critical one, the maximum amplitude of transverse displacement in the region of the free end of the beam is overestimated for higher airflow speeds.

For the mass ratio considered in the case studies of this paper, the modal form of LCOs of a plain steel beam in the post-critical regime is a complex deformation which is a combination of the first two bending modes (and hence is not a simple standing wave mode with a stationary strain node). As a result, the strain node travels substantially along the beam length during each cycle of oscillation. The theoretical predictions show that the spatial location of the strain node is not uniform with time during each cycle of persistent oscillations at each airflow speed. However, the strain node is mostly placed in a specific region (along the length) within a cycle, which can easily be located by averaging its position over the course of an oscillation cycle for each airflow speed. This dominant position is the segmentation point for a specific airflow

speed. The dominant position of strain nodes averaged over a range of airflow speeds with high amplitude LCOs results in the segmentation position (17% from the clamped end for the configurations in this work) to reduce the cancelation problem at different airflow speeds. The segmentation criterion is numerically demonstrated and experimentally validated for a PVDF bimorph in axial flow. The criterion proposed in this work yields more than 30% increase in the harvested power as compared to using a continuous piezoelectric cantilever.

Acknowledgments

This work was supported by the Sao Paulo Research Foundation (FAPESP), Brazil grant 2015/11325-3 and by the National Science Foundation, USA grant CMMI-1254262. We would like to thank Dr. David Hu at Georgia Tech for providing the high speed camera system.

References

Abdelkefi, A., Hajj, M.R., 2013. Performance enhancement of wing-based piezoaeroelastic energy harvesting through freeplay nonlinearity. Theoret. Appl. Mech. Lett. 3 (4).
Abdelkefi, A., Nayfeh, A., Hajj, M., 2012. Design of piezoaeroelastic energy harvesters. Nonlinear Dynam. 68 (4), 519–530.
Abdelkefi, A., Nayfeh, A., Hajj, M., 2012c. Modeling and analysis of piezoaeroelastic energy harvesters. Nonlinear Dynam. 67 (2), 925–939.
Bae, J., Inman, D., 2014. Aeroelastic characteristics of linear and nonlinear piezo-aeroelastic energy harvester. J. Intell. Mater. Syst. Struct. 25 (4), 401–416.
Bisplinghoff, R.L., Ashley, H., Halfman, R.L., 1996. Aeroelasticity. In: Dover Books on Aeronautical Engineering, Dover Publications, p. 880.
Bruni, C., Gibert, J., Frulla, E., Cestino, G., Marzocca, P., 2017. Energy harvesting from aeroelastic vibrations induced by discrete gust loads. J. Intell. Mater. Syst. Struct. 28 (1), 47–62.
De Marqui Jr., C., Erturk, A., 2013. Electroaeroelastic analysis of airfoil-based wind energy harvesting using piezoelectric transduction and electromagnetic induction. J. Intell. Mater. Syst. Struct. 24 (7), 846–854.
De Marqui Jr., C., Erturk, A., Inman, D.J., 2010. Piezoaeroelastic modeling and analysis of a generator wing with continuous and segmented electrodes. J. Intell. Mater. Syst. Struct. 21 (10), 983–993.
De Marqui Jr., C., Vieira, W.G.R., Erturk, A., Inman, D.J., 2011. Modeling and analysis of piezoelectric energy harvesting from aeroelastic vibrations using the doublet-lattice method. Trans. ASME, J. Vib. Acoust. 133 (1).
Dias, J., De Marqui Jr., C., Erturk, A., 2013. Hybrid piezoelectric-inductive flow energy harvesting and dimensionless electroaeroelastic analysis for scaling. Appl. Phys. Lett. 102 (4), 044101.
Dowell, E.H., Tang, D., 2002. Nonlinear aeroelasticity and unsteady aerodynamics. AIAA J. 40 (9).
Dunnmon, J., Stanton, S., Mann, B., Dowell, E., 2011. Power extraction from aeroelastic limit cycle oscillations. J. Fluids Struct. 27 (8), 1182–1198.
Erturk, A., Inman, D., 2008. A distributed parameter electromechanical model for cantilevered piezoelectric energy harvesters. Trans. ASME, J. Vib. Acoust. 130 (4).
Erturk, A., Inman, D.J., 2011. Piezoelectric Energy Harvesting. Wiley, Chichester, UK.
Erturk, A., Tarazaga, P.A., Farmer, J.R., Inman, D.J., 2009. Effect of strain nodes and electrode configuration on piezoelectric energy harvesting from cantilevered beams. J. Vib. Acoust. 131 (1), 011010.
Erturk, A., Vieira, W., De Marqui Jr., C., Inman, D., 2010. On the energy harvesting potential of piezoaeroelastic systems. Appl. Phys. Lett. 96 (18), 184103.
Guo, C., Paidoussis, M., 2000. Stability of rectangular plates with free side-edges in two-dimensional inviscid channel flow. J. Appl. Mech. 67 (1), 171–176.
Houbolt, J.C., 1950. A recurrence matrix solution for the dynamic response of elastic aircraft. J. Aeronaut. Sci. 17 (9), 540–550.
Huang, L., 1995. Flutter of cantilevered plates in axial flow. J. Fluids Struct. 9 (2), 127–147.
Javed, U., Dai, H., Abdelkefi, A., 2015. Nonlinear dynamics and comparative analysis of hybrid piezoelectric-inductive energy harvesters subjected to galloping vibrations. Eur. Phys. J. Spec. Top. 224 (14–15), 2929–2948.
Katz, J., Plotkin, A., 2001. Low Speed Aerodynamics, second ed.. In: Cambridge Aerospace Series, Cambridge University Press, Cambridge, UK, New York, xvi, 613.
Kornecki, A., Dowell, E., O'brien, J., 1976. On the aeroelastic instability of two-dimensional panels in uniform incompressible flow. J. Sound Vib. 47 (2), 163–178.
Pineirua, M., Doare, O., Michelin, S., 2015. Influence and optimization of the electrodes position in a piezoelectric energy harvesting flag. J. Sound Vib. 346, 200–215.
Semler, C., Li, G., Paıdoussis, M., 1994. The non-linear equations of motion of pipes conveying fluid. J. Sound Vib. 169 (5), 577–599.
Shang-Rou, H., Shaw, S.W., Pierre, C., 1994. Normal modes for large amplitude vibration of a cantilever beam. Int. J. Solids Struct. 31 (14), 1981–2014.
Shayo, L., 1980. The stability of cantilever panels in uniform incompressible flow. J. Sound Vib. 68 (3), 341–350.
Singh, K., Michelin, S., De Langre, E., 2012. The effect of non-uniform damping on flutter in axial flow and energy-harvesting strategies. In: Proc. R. Soc. A. The Royal Society.
Sousa, V.C., Anicezio, M.d.M., De Marqui Jr., C., Erturk, A., 2011a. Enhanced aeroelastic energy harvesting by exploiting combined nonlinearities: theory and experiment. Smart Mater. Struct. 20 (9).
Sousa, V., De Marqui, C., 2015. Airfoil-based piezoelectric energy harvesting by exploiting the pseudoelastic hysteresis of shape memory alloy springs. Smart Mater. Struct. 24 (12).
Tang, D.M., Dowell, E.H., 2002. Limit cycle oscillations of two-dimensional panels in low subsonic flow. Int. J. Non-Linear Mech. 37 (7), 1199–1209.
Tang, D.M., Dowell, E.H., 2018. Aeroelastic response and energy harvesting from a cantilevered piezoelectric laminated plate. J. Fluids Struct. 76, 14–36.
Tang, L., Paidoussis, M., 2007. On the instability and the post-critical behaviour of two-dimensional cantilevered flexible plate's in axial flow. J. Sound Vib. 305 (1–2), 97–115.
Tang, L., Paidoussis, M., 2008a. The dynamics of two-dimensional cantilevered plates with an additional spring support in axial flow. Nonlinear Dynam. 51 (3), 429–438.
Tang, L., Paidoussis, M., 2008b. The influence of the wake on the stability of cantilevered flexible plates in axial flow. J. Sound Vib. 310 (3), 512–526.
Tang, L., Paidoussis, M., 2009. The coupled dynamics of two cantilevered flexible plates in axial flow. J. Sound Vib. 323 (3–5), 790–801.
Tang, L., Paidoussis, M., Jiang, J., 2009a. Cantilevered flexible plates in axial flow: Energy transfer and the concept of flutter-mill. J. Sound Vib. 326 (1–2), 263–276.
Tang, L., Paidoussis, M., Jiang, J., 2009b. The dynamics of variants of two-dimensional cantilevered flexible plates in axial flow. J. Sound Vib. 323 (1–2), 214–231.
Tang, D., Yamamoto, H., Dowell, E., 2003. Flutter and limit cycle oscillations of two-dimensional panels in three-dimensional axial flow. J. Fluids Struct. 17 (2), 225–242.

Theodorsen, T., 1935. General theory of aerodynamic instability and the mechanism of flutter. In: NACA TR-496. Langley Memorial Aeronautical Laboratory.
Xiang, J., Wu, Y., Li, D., 2015. Energy harvesting from the discrete gust response of a piezoaeroelastic wing: Modeling and performance evaluation. J. Sound Vib. 343, 176–193.